68th International Astronautical Congress, Adelaide, Australia. Copyright ©2017 by the International Astronautical Federation. All rights reserved.

IAC-17, C4, 10, 11, x 39688

ADVANCEMENT OF ROCKET ENGINE PERFORMANCE THROUGH NOVEL APPROACHES FOR THRUST CHAMBER DESIGN

Markus Ortelt
German Aerospace Center (DLR), Germany, markus.ortelt@dlr.de

Hermann Hald
German Aerospace Center (DLR), Germany, hermann.hald@dlr.de
Stelios Michaelides
German Aerospace Center (DLR), Germany, stelios.michaelides@dlr.de
Helge Seiler
German Aerospace Center (DLR), Germany, helge.seiler@dlr.de
Georg Herdrich
University of Stuttgart, Germany, herdrich@irs.uni-stuttgart.de

The long lasting effort of the German Aerospace Center DLR in developing transpiration cooled thrust chambers made from ceramic matrix composites (CMC) has led to novel approaches for designing thrust chambers. A first innovation is a novel contour geometry, which is predicted to provide desirable properties in terms of peak heat flux and total heat load. Other innovations relate to the wall design and material. The approaches promise advantages in the following areas:

a) Film cooled orbital propulsion. The reduction of the peak heat flux reduces the necessary extend of film cooling and thus leads to a significant increase of the specific impulse and/or life time of the engine.

b) Expander cycle engines. The increase of the total heat flux at equal surface areas / thrust chamber volumes enables shorter thrust chambers. This allows for a reduced stage weight.

c) Classical gas generator engines. Using the new chamber contour, wall design and materials, the pressure loss caused by chamber cooling is removed. This seems to be the most significant improvement of the new design approach.

In conjunction with thermally safe inner wall surfaces, the latter allows for a high redundancy in terms of heat exchange management. In case of liquid oxygen / methane operation for instance, the potential of cost reduction is enhanced, because the engine efficiency does not depend on extremely clean methane. Liquid natural gas will not significantly affect the engine performance by decreased heat exchange management, caused by lower fuel quality. Additionally, several thermo-physical monitoring systems inside the hot gas plenum can simultaneously be operated safely, because the inner wall surface will not see any critical temperatures.

Such improvements could make CMC high performance rocket thrust chambers exceptionally attractive regarding the future growing market of governmental as well as private commercial space transportation.

I. INTRODUCTION

The *BlackEngine* development of DLRs ceramic rocket thrust chamber technology shows currently Technology Readiness Level five (TRL 5). At the end of 2013, all basic technological questions could be answered in separated detailed investigations, such that from that point on the focus was oriented to the evaluation of prospects for the industrial transfer and further technological improvement.

On the one hand DLR still follows the established concept line for the CMC (Ceramic Matrix Composites) TCA (Thrust Chamber Assembly), using transpiration cooling through inner CMC liners with classic contours [4÷9]. On the other hand, current design improvements accompany the entire engine development aiming at competitive advantages for future industrial application. This includes the investigation of a completely new chamber geometry approach, the dual hyperboloid contour design. This approach promises significant engine efficiency increase through the new injection cooling method, where the complete inner chamber wall operates as a porous fuel injector.

At the end of 2016 the German WEPA-Technologies acquired licenses for the CMC TCA technology as the first partner with industrial interest. WEPA-Technologies SME is currently expected to be the only completely private producer of high performance rocket turbo pumps (TP) in Germany. They are also an active partner in the current EU H2020 SMILE project.

 Copyright ©2017 by the International Astronautical Federation. All rights reserved.

Additionally, DLR collaborates actively with the institute of fluid mechanics and turbo-machines at the Technical University (TU) of Kaiserslautern, which is an institute of academic excellence in rotational pump technology. Beside the investigation of a new CMC journal bearing technology for cryogenic rocket turbo pumps, DLR creates in common with the University of Kaiserslautern and WEPA-Technologies a consortium for the demonstration of an entire 35 kN rocket propulsion system using liquid oxygen (LOX) and liquid methane (LCH4). This includes the DLR CMC TCA, the WEPA-Technologies turbo pump and the academic turbo-machine competency of TU-Kaiserslautern. Basic technological demonstration will be done in a small hot-firing test stand for sub-scale investigation, which is currently being built up.

II. CLASSICAL TCA APPROACH

The demonstration of an entire 35 kN LOX/LCH4 rocket engine is a challenging goal. Based on the TRL 5, a classic transpiration cooled thrust chamber design (fig. 1), for highly efficient, highly reliable, low fatigue and low weight rocket motors, can be implemented

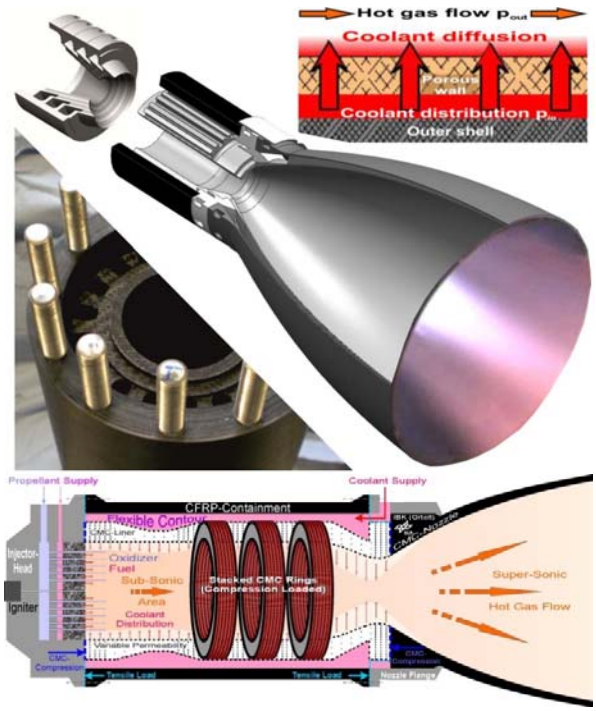

Fig. 1: Classical design of DLR's transpiration cooled CMC TCA. Top right: Transpiration principle. Middle: Structure design, incl. efficient bolt interface for metal-CFRP-joining. Bottom: Operational principal and de-coupled structure concept.

[4÷9]. A high ratio of de-coupling is given by the swimming structural design. Single CMC ring segments are inserted, one centred to the other, into the CFRP housing. Without being bonded to the outer housing, they are clamped together when mounting the flanges with the bolt interface. This provides a longer lifetime at low cost. Targeting the LOX/LCH4 application, several advantages are expected. Both propellants range at similar temperature levels. That principally makes the injector operation easier. Regarding the higher level of difficulty in the ignition of the LOX/LCH4 combination, DLRs' sophisticated engine start-up operation, using change of phase in the LOX injection element before ignition, helps for good mixing and ignition itself [16]. The specific cone injector design (fig. 2) with a rotationally symmetric injection pattern

Fig. 2: Concentric cone injector face-plate with alternating ring zones for fuel and oxidiser injection.

is characterised by alternating and concentric ring injection zones for fuel and oxidiser. The oxidiser injector elements are either manufactured from oxide CMC or SLM (Selective Laser Melting) parts. They show filigree inherent patterns of injector channels with small diameter of about 0.4 mm (fig. 3), whereas the fuel injection will be managed by thin gaps between the LOX injection elements. During the start-up phase, this

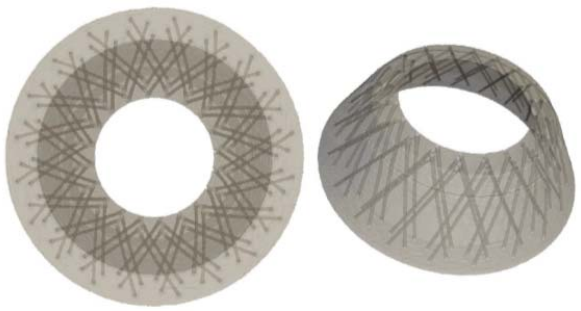

Fig. 3: Filigree channel arrangement inside the cone injector elements, via CMC or ALM design.

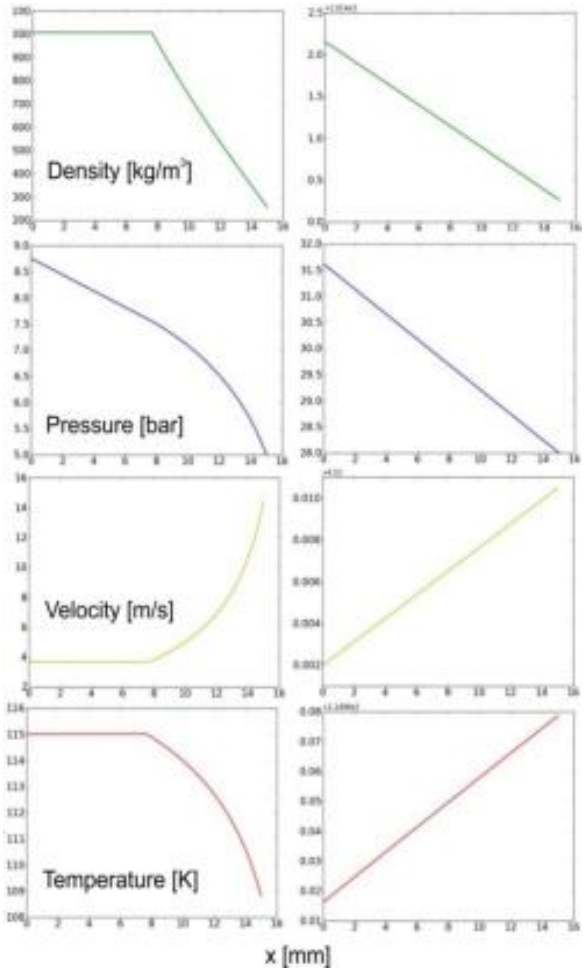

Fig. 4: Physical change from gaseous flow (left) before ignition to steady state operation (right) after ignition.

design allows a well-defined change of phase of the liquid oxygen to gas before ignition (fig. 4) as long as the counter-pressure on the combustion chamber side is low.

After the ignition, the chamber pressure rises quickly. The counter-pressure sustains the liquid oxidiser phase when passing the injection channels. From that point on the oxidiser flow is accompanied by a lower pressure drop at a high mass flow rate, which is what the steady-state phase requires.

Empirically inner porous combustion chamber walls attenuate combustion instabilities. In combination with the diffusion flame principle applied in the cone injector system a soft and stable combustion is predicted. This is supported by former test results at the European technology test facilities P8 and P6.1 at DLR Lampoldshausen.

Fig. 5: New double-shell CMC nozzle extension with high load de-coupling ratio.

Down-stream the sub-sonic combustion chamber a new double-shell CMC nozzle extension design has been added. The design (fig. 5) is characterised by a split of shells at the interface region. The inner shell carries the heat loads and the outer shell takes the mechanical loads. Using a fully transpiration cooled sub-sonic combustion chamber even under efficient cooling operation conditions has the inherent advantage that the accumulated residual coolant film, coming out from the nozzle throat, also cools the CMC nozzle extension automatically without any additional effort.

All the aspects mentioned previously promise a robust and failure tolerant, as well as a significantly simplified and cost reduced, TCA-system. The affiliation of three scientific-technological competencies, DLR, WEPA-Technologies and the TU-Kaiserslautern promises a successful trend-setting demonstration of an entire 35 kN rocket engine.

III. NOVEL TECHNOLOGY APPROACH

III.I Technology description

DLRs cone injector technology shows an enfolding hyperboloid injector spray shape, resulting from the injector channel outlet pattern following the generating lines of a typical one-shell hyperboloid geometry (fig. 6). The subsequent idea of a corresponding combustion chamber contour adaptation is obviously interesting. Firstly, the classical combination of a cylindrical and a convergent-divergent Laval nozzle is replaced by an injection-aligned wall contour (fig. 7, red).

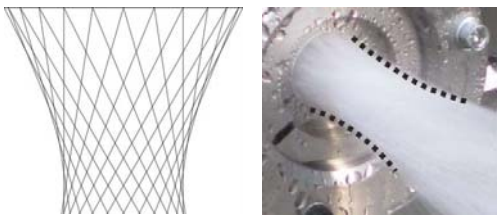

Fig. 6: Formation principle of the enfolding hyperboloid spray shape, following the generating lines coming from the injector outlet.

Principally such a geometry replacement leads to higher integrated heat transfer at the inner chamber wall, compared to the classical contour. However, considering that there exists a high amount of propellant injection through the porous wall, this aspect becomes less important. In combination with the diffusion flame principle, where multiple thin oxidiser jets spray into a fully formed fuel plenum, a soft and complete combustion can be expected. But, to bring the propellants into close contact, a reduction in volume, by inserting an inner core part (fig. 7, blue), improves the propellant mixing.

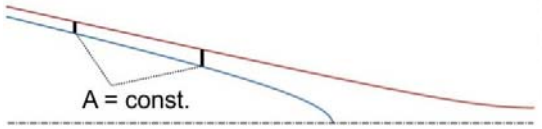

Fig. 7: Dual shell hyperboloid contour (upper half longitudinal section; left: injector side, right: nozzle throat side).

The resulting ring-shaped combustion chamber zone creates a concentrated mixing and combustion space. The requirement of a constant cross-sectional-area along the flow direction (fig. 7, quasi-cylindrical zone corresponding to the classical design) results in a partial two-shell hyperboloid at the inner core. Consequently, the constant cross-section-area turns at the end of the inner core automatically and harmonically into the convergent nozzle zone without any change of curve direction.

III.II Gas generator application

Typical applications of high fuel injection ratio are represented by both, fuel-rich pre-burners or gas generators for the turbo pump drive. The latter has been investigated numerically within diverse Ansys-CFX simulations, using LOX and LCH4 as propellants.

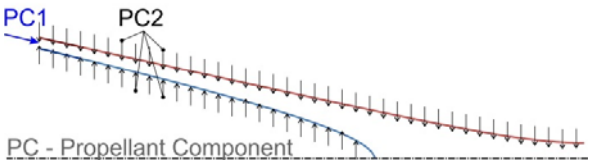

Fig. 8: Arrangement of the two-propellant propellant inflow.

Propellant component number 1 (fig. 8), LOX, will be injected exclusively through the thin face-plate zone, whereas component number 2, LCH4, will be completely injected via the porous dual-shell chamber walls.

Theoretical basics

The Navier-Stokes equations are represented by the conservation of momentum [1],

$$\frac{\partial(\rho\vec{v})}{\partial t} = -[\nabla\cdot\rho\vec{v}\vec{v}] - [\nabla\cdot\bar{\bar{\tau}}] - \nabla p + \rho\vec{g} \qquad [1]$$

extended by the continuity equation [2],

$$\frac{\partial\rho}{\partial t} = -div(\rho\vec{v}) \qquad [2]$$

and the energy equation [3]:

$$\frac{\partial}{\partial t}\left[\rho\cdot\left(e+\frac{1}{2}\cdot\vec{v}^2\right)\right] + \vec{\nabla}\left[\rho\cdot\vec{v}\cdot\left(h+\frac{1}{2}\cdot\vec{v}^2\right) - \tau\cdot\vec{v} - \lambda\cdot\vec{\nabla}T\right] = \rho\cdot\vec{g}\cdot\vec{v} \qquad [3]$$

The Stokes relations [system 4] couple stress and velocities with μ as dynamic viscosity:

$$\tau_{xx} = -\frac{2}{3}\mu\cdot\left(\frac{\partial u}{\partial x}+\frac{\partial v}{\partial y}+\frac{\partial w}{\partial z}\right) + 2\cdot\mu\cdot\frac{\partial u}{\partial x} \qquad [4]$$

$$\tau_{yy} = -\frac{2}{3}\mu\cdot\left(\frac{\partial u}{\partial x}+\frac{\partial v}{\partial y}+\frac{\partial w}{\partial z}\right) + 2\cdot\mu\cdot\frac{\partial v}{\partial y}$$

$$\tau_{zz} = -\frac{2}{3}\mu\cdot\left(\frac{\partial u}{\partial x}+\frac{\partial v}{\partial y}+\frac{\partial w}{\partial z}\right) + 2\cdot\mu\cdot\frac{\partial w}{\partial z}$$

$$\tau_{xy} = \mu\cdot\left(\frac{\partial v}{\partial x}+\frac{\partial u}{\partial y}\right)$$

$$\tau_{xz} = \mu\cdot\left(\frac{\partial w}{\partial x}+\frac{\partial u}{\partial z}\right)$$

$$\tau_{yz} = \mu\cdot\left(\frac{\partial v}{\partial z}+\frac{\partial w}{\partial y}\right)$$

The thermal equation of state couples density, pressure and temperature [5]:

$$p = \rho\cdot R\cdot T \qquad [5]$$

The caloric equations of state couple enthalpy, inner energy and temperature [system 6]:

$$de = c_v\cdot dT$$

$$dh = c_p\cdot dT \qquad [6]$$

The volume averaging of a Newtonian fluid in a porous media is described by Darcy-Forchheimer [7]:

$$\frac{dp}{dx} = -\left(\frac{\eta}{k_D}\cdot u + \frac{\rho}{k_f}\cdot u^2\right) \qquad [7]$$

The temperature distribution in the porous media, which is in non-equilibrium with the fluid phase is described by equation [8] in the solid and equation [9] in the fluid:

$$0 = \lambda_{s,e} \cdot \frac{d^2 T_s}{dx^2} - \alpha \cdot (T_s - T_f) \quad [8]$$

$$\dot{m} \cdot \frac{c_f}{A} \cdot \frac{dT_f}{dx} = \lambda_{f,e} \cdot \frac{d^2 T_f}{dx^2} + \alpha (T_s - T_f) \quad [9]$$

Here, α is the coefficient of volumetric heat transfer, $\dot{m}$ is the fluid mass flow and c_f is the fluid heat capacity. The thermal conductivity of the solid and the fluid is described by equations [10] and [11]

$$\lambda_{s,e} = (1 - \varepsilon) \cdot \lambda_s \quad [10]$$

$$\lambda_{f,e} = \varepsilon \cdot \lambda_f \quad [11]$$

The overall flow density of a multi-substance mixture is given in vector form by [12]:

$$\overrightarrow{\dot{m}_i} = \overrightarrow{\dot{m}_i}^{(KN)} + \overrightarrow{\dot{m}_i}^{(P)} + \overrightarrow{\dot{m}_i}^{(K)} + \overrightarrow{\dot{m}_i}^{(S)} \quad [12]$$

with Fick's concentration ratio [13]:

$$\overrightarrow{\dot{m}_i}^{(KN)} = \frac{c^2}{\rho} \sum_{k=1}^{n} \varsigma_i \varsigma_k D_{ik}{}^{(id)} \left[\frac{x_k}{RT} \sum_{i=1}^{n} \left(\frac{\partial \overline{G_k}}{\partial x_l} \right)_{T,p,x_s} grad\ x_l \right] \quad [13]$$

which is simplified to [14]:

$$\overrightarrow{\dot{m}_i}^{(KN)} = \frac{c^2}{\rho} \sum_{k=1}^{n} \varsigma_i \varsigma_k D_{ik}{}^{(id)} \left[\sum_{i=1}^{n} grad\ x_l \right] \quad [14]$$

with the following boundary condition for the diffusion coefficient [system 15]:

$$D_{ii}{}^{(id)} = 0$$
$$\sum_{i=1}^{n} (\varsigma_i \varsigma_h D_{ih}{}^{(id)} - \varsigma_i \varsigma_l D_{il}{}^{(id)}) = 0 \quad [15]$$

The flow density caused by pressure difference is given by [16]:

$$\overrightarrow{\dot{m}_i}^{(P)} = \frac{c^2}{\varrho} \sum_{k=1}^{n} \varsigma_i \varsigma_k D_{ik}{}^{(id)} \left[\frac{x_k \varsigma_k}{RT} \left(\frac{\overrightarrow{V_k}}{\varsigma_k} - \frac{1}{\rho} \right) grad\ p \right] \quad [16]$$

$\vec{V}_K$ is the partial Mol-volume of component k. Considering ideal gas [16] can be simplified with $\vec{V}_K = \frac{1}{c}$ to [17]:

$$\overrightarrow{\dot{m}_i}^{(P)} = \frac{c^2}{\varrho} \sum_{k=1}^{n} \varsigma_i \varsigma_k D_{ik}{}^{(id)} \left[\frac{\frac{x_k}{RT} \left(\frac{\rho_k^*}{x_k} - 1 \right) (grad\ p)}{p} \right] \quad [17]$$

with $\rho^*{}_K = \frac{\rho^*}{\rho}$ and [18] which couples density and mole fraction:

$$x_k = \frac{\rho_k^* / \varsigma_k}{\rho_k^* / \varsigma_k + (1 - \rho_k) / \varsigma_k} \quad [18]$$

The flow density caused by outer forces is given by:

$$\overrightarrow{\dot{m}_i}^{(K)} = -\frac{c^2}{\rho} \sum_{k=1}^{n} \varsigma_i \varsigma_k D_{ik}^{(id)} \left[\frac{x_k \varsigma_k}{RT} (\overrightarrow{g_k} - \sum_{l=1}^{n} \rho_l^* \overrightarrow{g_l}) \right] \quad [19]$$

The SORETIC [20] and convective [21] flow densities are given by:

$$\overrightarrow{\dot{m}_i}^{(S)} = -\frac{D_{Ti} (grad\ T)}{T} \quad [20]$$

$$\dot{m}_a = \beta A \Delta \rho_a \quad [21]$$

Using the previous relations the equation of the concentration field is represented by [22]:

$$\frac{D\rho_i}{Dt} = \frac{\partial \rho_i}{\partial t} + (\vec{v} \cdot \nabla \rho_i) = -\rho (\nabla \cdot \vec{v}) - \left(\nabla \cdot \overrightarrow{\dot{m}_i} \right) + \dot{r}_i \varsigma_i \quad [22]$$

with $\frac{\partial \rho_i}{\partial t}$ being the temporal mass increase per volume unit, $(\nabla \vec{v} \rho_i)$ and $(\nabla \overrightarrow{\dot{m}_i})$ are the temporal partial density gradients by convection and conduction, and $\dot{r}_i$ is the volume-related flow density, e.g. caused by homogeneous chemical reaction.

Combustion of LOX and LCH4

The basic reaction mechanism of oxygen and methane is given by [23]

$$CH_4 + 2O_2 \rightarrow CO_2 + 2H_2O \quad [23]$$

Regarding the gas generator application, a significantly under-stoichiometric mixture ratio has to be considered. Consequently other reactants occur, as given in [system 24]

$$2CH_4 + 3O_2 \rightarrow 2CO + 4H_2O$$
$$CH_4 + O_2 \rightarrow C + 2H_2O \quad [24]$$

The complete reaction chain is given in table 1.

The stoichiometric combustion enthalpy is represented by [25],

$$\Delta_R H^0 = \sum_{i=1}^{S} \nu_i H_{f,i}^0 = (-1(-74,85) + 0 + 1(-393,5) + 2(-241,81)) \frac{\text{kJ}}{\text{mol}} = -802,3 \frac{\text{kJ}}{\text{mol}} \quad [25]$$

The adjusted reduced enthalpy in this case can be found via CEA [10] or RPA [11].

No.	Reaction	Coefficient of velocity
1.	$CH_4 + M \rightarrow CH_3 + H + M$	$1{,}5 \times 10^{19} \cdot \exp(-50300/T)$
2.	$CH_4 + O_2 \rightarrow CH_3 + HO_2$	$1{,}0 \times 10^{14} \cdot \exp(-22700/T)$
3.	$O_2 + M \rightarrow 2O + M$	$3{,}6 \times 10^{18} \cdot T^{-1{,}0} \cdot \exp(-59400/T)$
4.	$CH_4 + O \rightarrow CH_3 + OH$	$1{,}7 \times 10^{13} \cdot \exp(-4380/T)$
5.	$CH_4 + H \rightarrow CH_3 + H_2$	$6{,}3 \times 10^{13} \cdot \exp(-6350/T)$
6.	$CH_4 + OH \rightarrow CH_3 + H_2O$	$2{,}8 \times 10^{13} \cdot \exp(-2500/T)$
7.	$CH_3 + O \rightarrow H_2CO + H$	$10^{13} - 10^{15}$
8.	$CH_3 + O_2 \rightarrow H_2CO + OH$	$10^{10} - 10^{14}$
9.	$H_2CO + OH \rightarrow HCO + H_2O$	$10^{13} - 10^{15}$
10.	$HCO + OH \rightarrow CO + H_2O$	$10^{12} - 10^{15}$
11.	$CO + OH \rightarrow CO_2 + H$	$3{,}1 \times 10^{11} \cdot \exp(-300/T)$
12.	$H + O_2 \rightarrow O + OH$	$2{,}2 \times 10^{14} \cdot \exp(-8310/T)$
13.	$O + H_2 \rightarrow H + OH$	$4{,}0 \times 10^{14} \cdot \exp(-4730/T)$
14.	$O + H_2O \rightarrow 2OH$	$8{,}4 \times 10^{14} \cdot \exp(-9120/T)$
15.	$H + H_2O \rightarrow H_2 + OH$	$1{,}0 \times 10^{14} \cdot \exp(-10200/T)$
16.	$H + OH + M \rightarrow H_2O + M$	$2{,}0 \times 10^{19} \cdot T^{-1{,}0}$
17.	$CH_3 + O_2 \rightarrow HCO + H_2O$	$10^{10} - 10^{12}$
18.	$HCO + M \rightarrow H + CO + M$	$2{,}0 \times 10^{13} \cdot T^{0{,}5} \cdot \exp(-14400/T)$

Table 1: Basic mechanism of the CH_4 / O_2 reaction.

Averaged Navier-Stokes equations and numerical adaptation in Ansys CFX

The averaged Navier-Stokes equations can be given as the addition of low and high frequent fluctuation systems for the single magnitudes ρ, u, v, w, e, as given in [system 26]:

$$\rho = \overline{\rho} + \rho'$$
$$u = \overline{u} + u'$$
$$v = \overline{v} + v' \qquad [26]$$
$$w = \overline{w} + w'$$
$$e = \overline{e} + e'$$

The practical simplification consists, on the one hand, of the use of only low frequent magnitudes and, on the other hand, of the use of using simplified turbulence models, like the k-ε-model, the k-ω-model, or the SST model in the boundary layer.

The k-ε-model comprises the relations [22] and [23]:

$$\mu_{eff} = \mu + \mu_t \qquad [22]$$

$$\mu_t = C_\mu \rho \frac{k^2}{\varepsilon} \qquad [23]$$

Hereby the turbulent viscosity μ_t and the turbulent kinetic energy k are coupled through [23]. These equations describe the development of the turbulent kinetic energy k and the isotropic dissipation ratio [24]:

$$\varepsilon = \nu \overline{\left(\frac{\partial u_i'}{\partial x_k}\right)\left(\frac{\partial u_i'}{\partial x_k}\right)} \qquad [24]$$

For their calculation additionally [25] and [26] will be used:

$$\rho \frac{\partial k}{\partial t} + \rho \overline{u_j} \frac{\partial k}{\partial x_j} = C_\mu \rho \mu_t \left(\frac{\partial \overline{u_i}}{\partial x_j} + \frac{\partial \overline{u_j}}{\partial x_i}\right) \frac{\partial \overline{u_i}}{\partial x_j} - \rho\varepsilon + \frac{\partial}{\partial x_j}\left[\left(\mu + \frac{\mu_t}{\sigma_k}\right)\frac{\partial k}{\partial x_j}\right] \qquad [25]$$

$$\rho \frac{\partial \varepsilon}{\partial t} + \rho \overline{u_j} \frac{\partial \varepsilon}{\partial x_j} = \frac{C_{\varepsilon 1}\varepsilon}{k} \tau_{ij} \frac{\partial \overline{u_i}}{\partial x_j} - \frac{C_{\varepsilon 2}\varepsilon^2}{k} C_\mu \rho \mu_t \left(\frac{\partial \overline{u_i}}{\partial x_j} + \frac{\partial \overline{u_j}}{\partial x_i}\right) \frac{\partial \overline{u_i}}{\partial x_j} - C_{\varepsilon 2}\rho \frac{\varepsilon^2}{k} + \frac{\partial}{\partial x_j}\left[\left(\mu + \frac{\mu_t}{\sigma_\varepsilon}\right)\frac{\partial \varepsilon}{\partial x_j}\right] \qquad [26]$$

$C_{\varepsilon 1}$, $C_{\varepsilon 2}$, σ_k, σ_ε and C_μ are constant. The k-ε-model describes accurately the inner core flow, but it shows deficits in the near-wall-region. Therefore the k-ω-model approximates more accurately the turbulence close to the wall, which uses the turbulent frequency ω instead of the turbulent dissipation ε. Showing lower boundary layer resolution it delivers acceptable results of the turbulence approximation. But in the core flow it shows deficits. The turbulence here will be modelled on the one hand by transport equation [28] for the turbulent energy k and on the other hand [29] for the characteristic frequency [27] of the dissipating turbulence

$$\omega = \frac{\frac{1}{C_\mu}\varepsilon}{k} \qquad [27]$$

$$\rho \frac{\partial k}{\partial t} + \rho \overline{u_j} \frac{\partial k}{\partial x_j} = C_\mu \rho \mu_t \left(\frac{\partial \overline{u_i}}{\partial x_j} + \frac{\partial \overline{u_j}}{\partial x_i}\right) \frac{\partial \overline{u_i}}{\partial x_j} - \beta^* \rho k \omega + \frac{\partial}{\partial x_j}\left[(\mu + \sigma^* \mu_t)\frac{\partial k}{\partial x_j}\right] \qquad [28]$$

$$\rho \frac{\partial \omega}{\partial t} + \rho \overline{u_j} \frac{\partial \omega}{\partial x_j} = \frac{\alpha \omega}{k} C_\mu \rho \mu_t \left(\frac{\partial \overline{u_i}}{\partial x_j} + \frac{\partial \overline{u_j}}{\partial x_i}\right) \frac{\partial \overline{u_i}}{\partial x_j} - \beta \rho \omega^2 + \frac{\partial}{\partial x_j}\left[(\mu + \sigma \mu_t)\frac{\partial \varepsilon}{\partial x_j}\right] \qquad [29]$$

C_μ comes from the k-ε-model. C_μ, α, β, σ, β* and σ* are the constants closing the system of equations.

The SST-model (shear-stress-transport) combines the advantages of the k-ε-model in the core flow region and of the k-ω-model in the near-wall-region.

Principally the boundary layer can be divided into two zones, the quasi-laminar near-wall-zone and the logarithmically approximated turbulent wall-distanced-zone. Consequently the near-wall-zone can be described by an empirical approximation (*wall-function-law*), given in [system 30]:

$$u^+ = \frac{U_t}{u_\tau} = \frac{1}{k}\ln(y^+) + C$$

$$y^+ = \frac{\rho \Delta y u_\tau}{\mu} \qquad [30]$$

$$u_\tau = \left(\frac{\tau_\omega}{\rho}\right)^{\frac{1}{2}}$$

u^+ is the velocity nearest to the wall, u_τ the friction velocity and U_t the velocity Δy far from the wall. τ_ω is the wall shear stress, k a constant defined by Karman [18], and C a constant depending on the wall roughness. Furthermore, y^+ is a non-dimensional wall distance, where the logarithmical wall-function-law can be applied in the range of $30 < y^+ < 300$. All turbulence models of Ansys-CFX are applicable for the wall-function-law. The most significant advantage of this method is the low-resolution mesh. Apart from this there is no need for the evaluation of the viscosity effects in the turbulence model.

The intermediate zone will be approximated by the *method of low Reynolds numbers*, where the k-ω-model and the SST-model are applicable. CFX developed an automated wall-function showing a smooth transition from the wall-function-law to the low Reynolds numbers method without losing approximation accuracy.

The temperature boundary layer will be managed by the approach [31] of reference [13]:

$$T^+ = Pry^* e^{-\Gamma} + [2.12\ln(y^*) + \beta]e^{-\frac{1}{\Gamma}} \qquad [31]$$

The following definitions [system 32] will be used in conjunction with [31]:

$$y^* = \frac{\frac{u^* \Delta y}{4}}{\upsilon}$$

$$u^* = C_\mu^{\frac{1}{4}} k^{\frac{1}{2}}$$

$$\beta = \left(3{,}85Pr^{\frac{1}{3}} - 1{,}3\right)^2 + 2{,}12\ln(\mathrm{Pr}) \qquad [32]$$

$$\Gamma = \frac{0{,}01(Pry^*)^4}{1+5Pr^3 y^*}$$

$$Pr = \frac{\mu c_p}{\lambda}$$

The influence of the wall roughness can lead to the transition from a laminar boundary layer to a turbulent one.

The resulting logarithmical velocity profile is given in [33]:

$$u^+ = \frac{1}{k}\ln(y^+) + B - \Delta B \qquad [33]$$

Constant B amounts to 5.2. ΔB is a function of the non-dimensional wall-roughness h^+, which is defined by [34]:

$$h^+ = \frac{h u_\tau}{\upsilon} \qquad [34]$$

Typical sand roughness is given by [35]:

$$\Delta B = \frac{1}{k}\ln(1 + 0{,}3h_s^+) \qquad [35]$$

With respect to the temperature influence on rough walls the adjusted wall-law is given by [36]:

$$T_{log}^+ = 2{,}12\ln(Pry^*) + \left(3{,}85Pr^{\frac{1}{3}} - 1{,}3\right)^2 - \Delta B_{th} \qquad [36]$$

using [37]:

$$\Delta B_{th} = \left(\frac{1}{0{,}41}\right)\ln(1 + C * 0{,}3Prh_S^+) \qquad [37]$$

C is an empirically acquired constant as seen in [14]. E.g. for the gaseous media air, C amounts to 0.2.

Concerning combustion the Eddy-Dissipation-Model is applied, which will often be used in simplified turbulent reactive flow, where the reaction velocity is high, compared to other transport processes. This model does not fit reaction kinetics, e.g. the transient ignition. The basis of the combustion models in Ansys CFX 17.1 [15] is the equation of the concentration field for multi-component mixture including sources for the chemical reactions in the form of [38]:

$$\frac{\partial(\rho\xi_I)}{\partial t} + \frac{\partial(\rho u_j \xi_I)}{\partial x_j} = \frac{\partial}{\partial x_j}\left(D_{Ieff}\frac{\partial \xi_I}{\partial x_j}\right) + M_I \qquad [38]$$

M_I is the mass source (sink) of component I, ξ_i the concerning mass fraction of component I in the fluid. The effective diffusion coefficient of component I is $D_{Ieff} = D_{It} + D_I$.

The chemical reactions are represented by a row of k elementary reactions witn N_C components through [39]:

$$\sum_{I=A,B,C,\ldots}^{N_C} \nu'_{kI}\, I \Leftrightarrow \sum_{I=A,B,C,\ldots}^{N_C} \nu''_{kI} I \qquad [39]$$

Herein ν_{kI} is the stoichiometric coefficient of component I in the elementary reaction k, ν'_{kI} refers to

the educts and ν''_{kl} to the products. The sum of all reaction ratios is given in [40]:

$$M_I = \varsigma_I \sum_{k=1}^{K} (\nu'_{kI} - \nu''_{kI})\, R_k \qquad [40]$$

Herein ς_I is the molar mass of component I and R_k the reaction ratio of the elementary reaction k, which will be calculated via the Eddy-Dissipation-Model in Ansys CFX 17.1.

In turbulent flow the mixture-time depends on the properties of the turbulence. For this reason the reaction ratio is proportional to the mixture time, which is given by the turbulent kinetic energy k and the dissipation ε [41]:

$$R_k \sim \frac{\varepsilon}{\kappa} \qquad [41]$$

Related to the Eddy-Dissipation-Model the reaction ratio of the elementary reaction k will be described by the lesser of the following expressions [system 42]:

$$R_k = \frac{A\varepsilon}{k} \min\left(\frac{[I]}{\nu'_{kI}}\right)$$
$$R_k = AB\frac{\varepsilon}{\kappa}\left(\frac{\sum_P (I)\varsigma_I}{\sum_P \nu''_{kI}\varsigma_I}\right) \qquad [42]$$

[I] is the molar concentration of component I, whereas I include only educts. P comprises all elementary reactions k. Constants A and B are empirical constants with the values 4 and 0.5.

This model is developed for a wide application range. Ansys CFX 17.1 can also limit the flame temperature. Hereby the reaction ratio will be "0" in case the limit temperature will be reached. This will be managed by two additional boundary conditions [system 43]:

$$R_{k,MFT} = A\frac{\varepsilon}{k} C_{MFT}$$
$$C_{MFT} = \max\{(T_{max} - T), 0[K]\} \cdot \frac{\rho C_P}{\Delta H_R} \qquad [43]$$

C_{MFT} is an imaginary concentration, which decreases to "0" in case of maximum temperature. C_P is the isobaric specific heat and ΔH_R the molar reaction enthalpy.

The model for porous media in Ansys CFX 17.1 uses Darcy's law. The model includes the advection term and the diffusion term. The derivation of the continuity equation assumes on the one hand large control volume, compared to the pore dimension, but on the other hand to be small, compared to the overall model. It will be described by the following two energy equations [system 44]:

$$\frac{\partial(\rho_s(1-\varepsilon)\alpha_s)}{\partial t} + \nabla \cdot (\rho_s K_s U_s \alpha_s) =$$
$$= \nabla \cdot (\lambda_s K_s \nabla T_s) + (1-\varepsilon) S_{Es} + Q_{sf} \qquad [44]$$
$$\frac{\partial(\rho\varepsilon\alpha)}{\partial t} + \nabla \cdot (\rho K U \alpha) = \nabla \cdot \left(\lambda_f K \nabla T\right) + \varepsilon S_{Ef} + Q_{fs}$$

The first one describes the solid, where the fluid diffuses. K is the area porosity tensor, U the velocity, S_E the heat source, and Q_{sf} the heat transferred from solid to fluid.

$$Q_{fs} = -Q_{sf} = \alpha_v S(T_S - T_F) \qquad [45]$$

The two energy equations are coupled by the coefficient of volumetric heat transfer α_v, which results from the specific surface area S and the coefficient of inner heat transfer between fluid and solid h_s.

$$\alpha_v = S \cdot \alpha_s \qquad [46]$$

These equations accept a local thermal non-equilibrium. Consequently two different temperatures for solid and fluid can be calculated at one location inside the porous medium. The temperature difference depends on the coefficient of volumetric heat transfer and it tends to "0" for large values.

Gas generator modelling

The comparison of direct inlet and transpiration operated [12] wall led finally to the decision of the latter, which models, in Ansys CFX 17.1, the wall shear stress behaviour best. In addition the modelling of source terms along the wall was combined with setting of friction.

DLRs development partner WEPA Technologies defined the operational parameters of the gas generator outlet targeting on the LOX / LCH4 turbo pump for a 35 kN rocket engine. Mass flow, mixture and contraction ratio as well as the chamber pressure were determined by RPA [11].

Six geometry variations have been investigated.

Numeric results

Six geometric configurations have been investigated. Figure 9 shows firstly the geometric variation, whereas the qualitative evaluation will show the method of how to find the geometric optimum. Case 5 of 6 fits the functional request best and will be discussed in the following section.

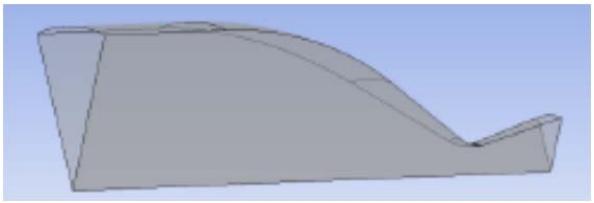

Case No. 1

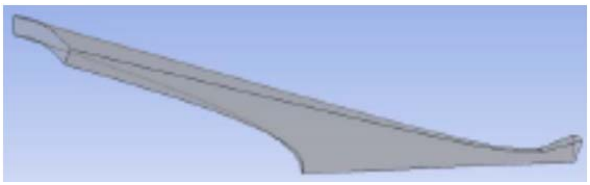

Case No. 2

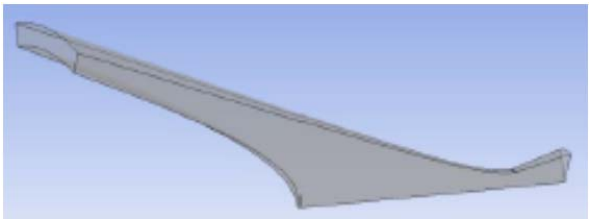

Case No. 3

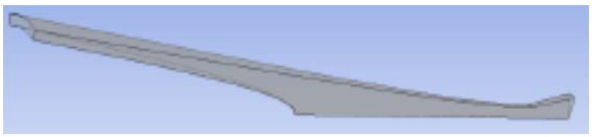

Case No. 4

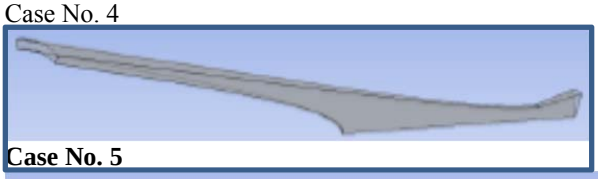

Case No. 5

Case No. 6

Fig. 9: Geometric variation of the gas generator chamber design.

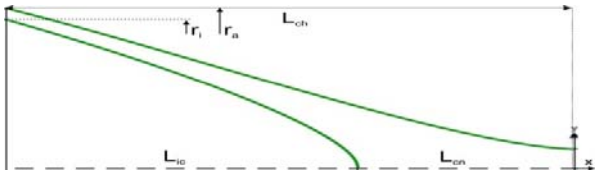

Fig. 10: Dimensions of the dual-shell hyperboloid gas generator chamber.

Fig. 9 shows highlighted the model cut-out of geometry case No. 5. The definition of the chamber geometry in principle bases on the operational boundary conditions given from WEPA-Technologies, the producer of the corresponding turbo pump system. The operational chamber pressure amounts to 54 bar, the mass flow to 400 g/s, static exit pressure and exit velocity to 3 bar and 1200 m/s. The final geometry, contraction (10.64) and mixture ratio (0.27) have been calculated by RPA. The one-shell hyperboloid follows equation [47], exhibits rotational symmetry and in two dimensions is found from [system 48], for this application (fig. 10):

$$\frac{y^2}{b^2}+\frac{z^2}{c^2}-\frac{x^2}{a^2}=1. \qquad [47]$$

$$\frac{y^2}{b^2}-\frac{x^2}{a^2}=1$$
$$r(x=0)=\frac{b}{a}\cdot\sqrt{a^2+0^2}=b=r_t \qquad [48]$$

The characteristic combustion chamber length is defined by [49]:

$$L^*=\frac{V_{ch}}{A_t} \qquad [49]$$

The concrete dimension is r_a = 45 mm and the total chamber length is L_{ch} = 200 mm. The latter orients on the experience of the former technology research for the transpiration cooled CMC TCA [3], where the characteristic chamber length amounted to 1.76 m. Slightly following the tendency towards lower L*, as seen in established full-scale chambers, but also using the latest research, the final used value was approximately 1.6 m. Table 2 shows the relevant chamber geometry.

	L_{ch} [mm]	L_{ic} [mm]	L_{cn} [mm]	L* [m]
Value	200.0	123.61	76.39	1.637
	r_t [mm]	ε	a [mm]	
Value	4.605	10.64	24.6	

Table 2: Relevant dimensions of the gas generator chamber.

Propellant component PC1 (oxidizer) amounted to 0.085 kg/s. The inner fuel injection (PC2 inner) amounted to 0.2 kg/s and PC2 outer to 0.115 kg/s. The coefficient of heat transfer amounted to α = 4285 W /m^2 K, and the ambient temperature was defined to be 300 K. Figure 11 shows the distribution of pressure, temperature and exit velocity in the geometric configuration with the best operational fit (case 5).

Comparing the shapes of the six different cases one interesting property found is the fact that the geometric optimum quotient of L_{ic} and L_{cn} lies in the golden

section (Φ =1.618) in case 5. Whether this be a coincidence shall be investigated in future development. Of course, the golden section would be a very interesting design guide value whether it could be proven in conjunction with this design approach.

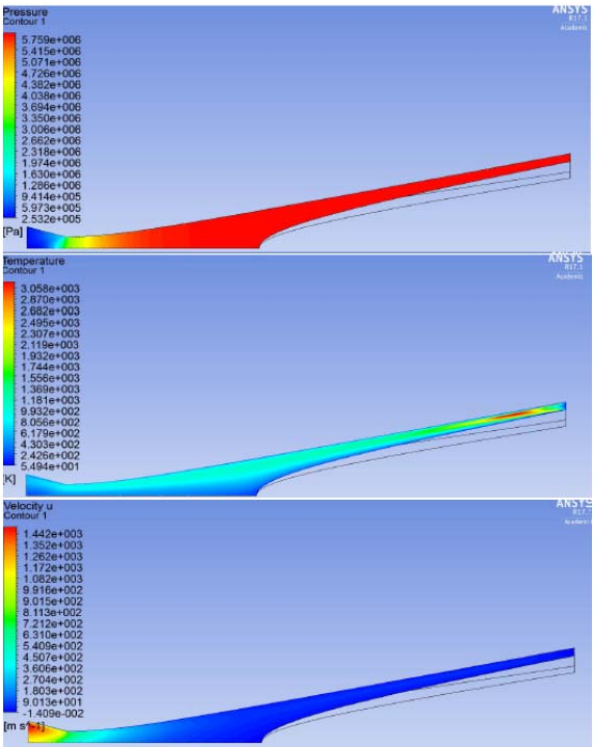

Fig. 11: Numerical results of the gas generator operation, case No. 5 (best geometrical fit, displayed mirror-inverted).

Structure analysis

The new rocket combustion chamber design investigates whether a dual hyperboloid combustion chamber design, made of the latest fibre-reinforced composites (carbon fibre-reinforced plastics CFRP and CMCs), can be used as a gas generator as well as for main combustion chambers. For the structural design of a hyperboloid gas generator combustion chamber, of a 35 kN LOX/LCH4 rocket propulsion system, special features of the design are taken into consideration. Its central combustion chamber component, consisting of a one-sheet hyperboloid outer contour and half of a two-sheet hyperboloid inner core, forms a ring combustion chamber zone in the start-up region, which is intended to enable the injection of the fuel to occur completely through the combustion chamber walls. For this purpose, the oxidizer is injected only through the end face of the injector, which is designed in the shape of a cone injector (current DLR research object). For a better fuel processing, two trace film cooling notches were implemented close to the oxidizer injector element (Injector-PIT). In case of an unexpected hotspot they provide a cooling opportunity and also the advantage of a pre mixing of the fuel components. All other ceramic parts are operated at non-critical operating temperature by using a fuel transpiration cooling system. The outer ceramic and the distributor sleeve are inside the CFRP housing. The connection between injector and nozzle is done through the bolt interface. For the two-sheet hyperboloid inner core a special screw made out of INCONEL® 718 had to be developed for full functionality of the inner core. A first thermal analysis with a short pre cooling phase showed that the forces are too high for all parts. Therefore a longer pre cooling phase is necessary. With the longer pre cooling and additional expansion gaps, normal operation is possible (fig. 12). These design modifications were necessary due to the gas generator being smaller than a full scale combustion chamber.

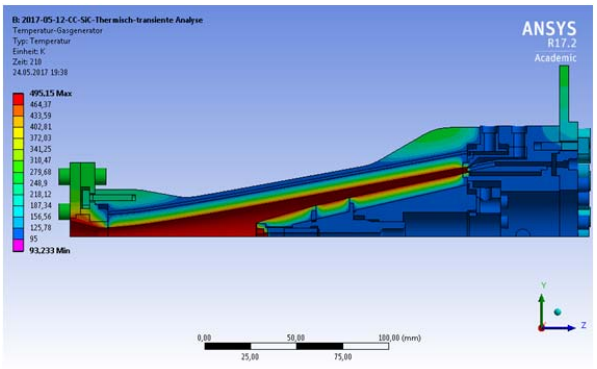

Fig. 12: Temperature plot of the transient thermo-mechanic analysis.

Discussion of results

By further balancing and optimisation of the propellant distribution on the injection surfaces, the potential is expected to reach homogeneous temperature fields across the exit plane without additional effort like distribution grids [17] as shown in figure 13.

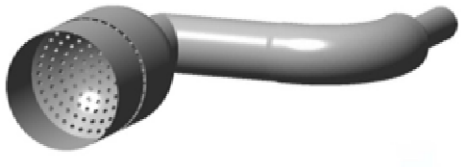

Fig. 13: Established hot gas distributor grids in rocket gas generators for homogeneous temperature fields.

III.III Application potential for orbital propulsion

The reliability of the engine is the most important constraint for orbital propulsion systems. This leads to the widespread usage of radiation cooled rocket engines that burn hypergolic fuels. The operation regime of this type of engines is limited by the thermal, mechanical and chemical stability of the thrust chamber and nozzle materials. These properties highly depend on the temperature. Subsequently, the maximum temperatures are the limiting factor and the operation regime is extended by film cooling. As the highest heat fluxes occur in the throat of the engine, the temperatures of the throat limit the operation regime despite the other parts of the engine operating far below acceptable temperature limits.

The analytical Bartz equation estimates the heat flux distribution in classical chamber geometries. It predicts a decrease of the heat fluxes in the throat with increasing radius of curvature. A high radius of curvature in the throat is typical for the hyperboloid chamber contour. A potential benefit can therefore be expected for the hyperboloid shape in terms of maximum throat temperature. This benefit would allow for higher service times or an extension of the operation regime with better mixing ratio or lower passive cooling mass flow rate with subsequently higher resulting specific impulse I_{SP}. The heat flux and temperature distribution are investigated in [2]. The diploma thesis provides the analytical functions for the investigated chamber geometries, the Bartz equation results and preliminary numerical results. The European Apogee Motor (EAM) is used as test case. The data presented in the following is summarized from this work.

A first estimation is gathered by solving the Bartz equation. The analytical geometry of the classical contour is modelled assuming a cylindrical chamber section followed by a convergent section that can be described by circle segments. The geometry is displayed in figure 14. The resulting analytical equation is [50]:

$$r(x) = \begin{cases} r_{ch}, & for\ -L_{ch} \le x < -L_{cn} \\ r_{ch} - R_{th} + \sqrt{R_{th}^2 - (L_{cn}+x)^2}, & for\ -L_{cn} \le x < -\frac{L_{cn}}{2} \\ r_{th} + R_{th} - \sqrt{R_{th}^2 - x^2}, & for\ -\frac{L_{cn}}{2} \le x < 0 \end{cases} \quad [50]$$

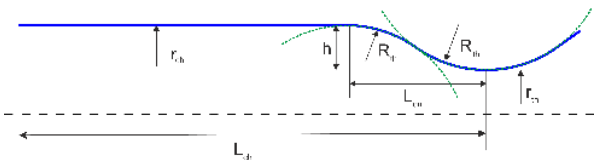

Figure 14: Classical chamber geometry.

The dimensions of the shape are estimated based on common design rules and the official working conditions. From the mass flow and total pressure, the throat diameter of 9.5 mm is calculated. The value is rounded up to regard the displacement thickness of the boundary layer. The radius and length of the cylindrical section are calculated based on the assumption of a contraction ratio of 4 and a chamber length of 150 mm. The characteristic length of the chamber is therefore 550 mm. The radius in the cylindrical section is to 19 mm.

The hyperboloid shape needs to reproduce the characteristic chamber dimensions. The throat diameter and chamber length are therefore set to the same values. The chamber geometry is provided in figure 15. The analytical description of the geometry is [51]:

$$r(x) = \frac{r_{th}}{a}\sqrt{a^2 + x^2}\,. \qquad a = \frac{L_{ch}}{\sqrt{\epsilon - 1}}\,. \quad [51]$$

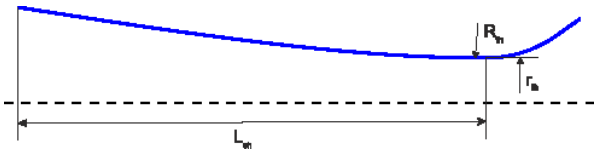

Figure 15: Hyperboloid chamber geometry.

This gives a contraction ratio of 9. The radius of curvature in the critical cross-section is 296 mm. This is huge compared to the radius of curvature of 26 mm in case of classical geometry.

The results of the Bartz equation show a significant reduction of the maximum heat flux in the throat region. However, the equation was derived for classical chamber contours and the applicability for hyperboloid shapes is questionable. Furthermore, the fact that there needs to be a lower limit of the scaling factor originating from the throat curvature radius is obvious. The results are presented in figure 16.

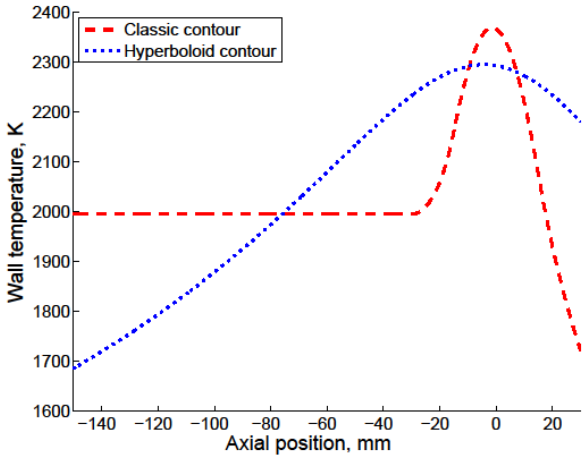

Figure 16: Analytical wall temperature distribution for the ideal engine.

The doubts are proven to be justified by the numerical simulations carried out using Ansys CFX. The simulations use several more or less restricting simplifications as ideal gas and non-reacting flow assumptions. The difference in the temperature distribution is very obvious (figure 17). It has to be pointed out, that the numerical results contradict the Bartz equation. The throat temperatures are higher for the hyperboloid shape. The behaviour is explained by the continuous acceleration of the flow that prevents the development of a thick boundary layer.

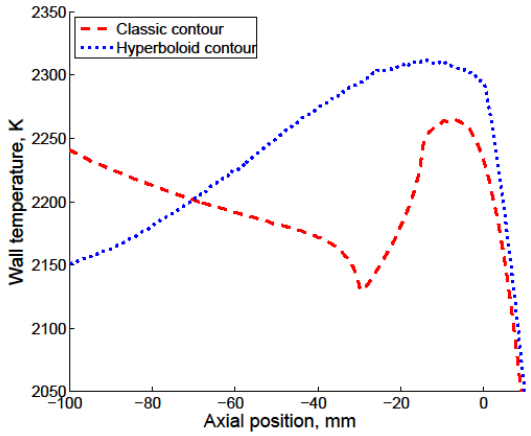

Figure 17: Numerical wall temperature distribution for the ideal engine.

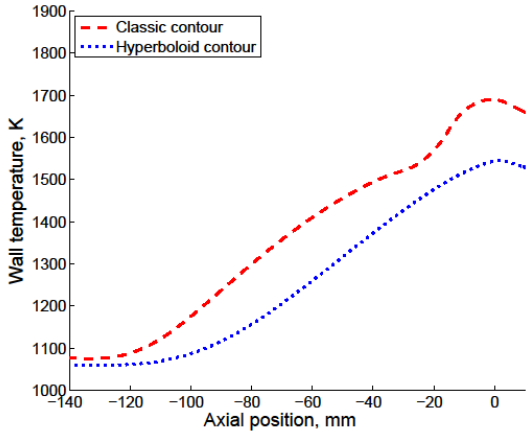

Figure 18: Numerical wall temperature distribution for the film cooled EAM.

The results suggest that the hyperboloid shape could be beneficial in case of film cooling. Subsequent simulations show the expected reduction of the throat temperature. The phenomenon originates from the different development of the boundary layer. As previously mentioned, the continuous acceleration leads to a thinner boundary layer. This stabilises the cooling film and increases its cooling efficiency. Please note that the modelled mass flow of the film cooling for the EAM is quite high. The usage of one fourth of the fuel is assumed. The results are given in figure 18.

According to the numerical results, the hyperboloid shape provides lower throat temperatures for the operation with thick cooling films.

III.IV Application potential for expander cycle engines

The results of the previous section predict a higher heat flux for the hyperboloid shape. Furthermore, the heat flux is distributed more smoothly. These properties are desirable for the operation of expander cycle engine, as they require a sufficiently high heat transfer through the chamber wall and the heat flux peaks of the classical contour are challenging for the dimensioning of the cooling system. The potential benefits of the hyperboloid shape for expander cycle engines are therefore investigated in the diploma thesis [2]. The data presented in this section is a summary of the according parts of that thesis. The Vinci engine is used as test case.

A shorter rocket engine allows a shorter adapter between two stages and is therefore desirable. To allow for this length reduction, additional to the classical and hyperboloid shapes, a hyperboloid shape with insert is investigated. The analytical equation [52] of the insert is derived from the demand of constant cross section area in the respective chamber segment. The shape is displayed in Figure 19.

$$r_i(x) = \begin{cases} \frac{r_{th}}{\bar{a}} \sqrt{\bar{a}^2 (1-\epsilon) + x^2}\,, & \text{for } x < -L_{cn} \\ 0, & \text{else}\,. \end{cases} \quad [52]$$

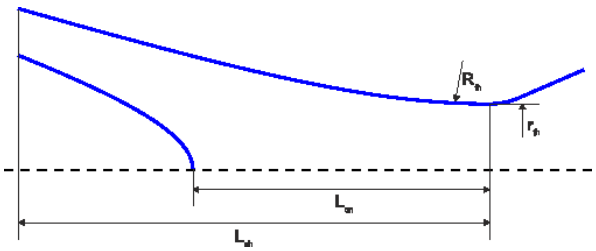

Figure 19: Geometry of the hyperboloid chamber with insert.

The throat radius is assumed to be 70 mm, the radius of the cylindrical segment of the classical chamber is set to 110 mm and the total chamber length is set to 630 mm. The hyperboloid shapes with and without insert are constructed with the same throat diameter and chamber length providing the same characteristic length.

The analytical results of the Bartz equation again predict lower heat fluxes for the hyperboloid shapes. Since the discrepancy between the Bartz equation and the numerical results is already discusses in the previous section, they are not presented here.

The numerical results for the heat fluxes depend on the wall roughness and scale by a factor of two between smooth and very rough wall. The values mentioned in the following take into account only the results for the medium roughness. The classical and hyperboloid chambers are very close with the classical contour providing 22.4 MW and 20.5 MW for the hyperboloid chamber. The advantage is thus on the side of the classical contour. This is also true for the maximum heat flux, which with 100 MW/m² is significantly higher for the hyperboloid. The classical shape has a maximum heat flux of 89 MW/m². The results look more promising when looking at the hyperboloid shape with insert. The total heat flow rises to 36.3 MW at the same chamber length and the maximum heat flux falls to 87 MW/m².

The advantages in the comparison shift towards the hyperboloid shapes when regarding, that the reaction of the fuels take some time. By assuming, that the first quarter of the chamber volume does not contribute to the heat flow because of still-cold gas, the total heat flow of the classical contour falls to 14.6 MW. The heat flow is also reduced for the hyperboloid, but the reduction is less significant. This is because the cross section area of the hyperboloid is larger near the injector. The resulting heat flow is thus higher than for the classical contour (19.5 MW). The advantage of the hyperboloid with insert rises further (29.4 MW).

The introduction of an insert for intensification of the heat transfer or shortening of the chamber seems to be feasible. The fact, that this approach significantly increases the engine weight and complexity, however, has to be regarded.

III.V Optical sensors on transpiration operated surfaces

During the phase of basic investigations on transpiration cooling in CMC rocket thrust chambers, one major question was the measurement of inner wall surface temperatures. Therefore the Institute of Space Systems at the University of Stuttgart contributed optical measurement by the use of its PYREX system, a one-color pyrometer operated with its own algorithm for data recording and sampling (equation [53], 'wand = wall') in logarithmic decades. For a wave-length range of around 850 nm, the system has been applied in micro-combustor chambers with 30 mm diameter and 10 bar chamber pressure. The O2-H2 mixture ratio amounted to 6.5.

$$\frac{dI_{Photo}}{d\lambda} = \left[L_{Wand}(\lambda, T_{Wand}(t)) + L_{Gas}(\lambda, T_{Gas})\right] f(\lambda)$$

$$I_{Photo} = \int_0^{\infty} \left[L_{Wand}(\lambda, T_{Wand}(t)) + L_{Gas}(\lambda, T_{Gas})\right] f(\lambda)\, d\lambda \qquad [53]$$

$$I_{Photo} = \int_0^{\infty} L_{Wand}(\lambda, T_{Wand}(t))\, f(\lambda)\, d\lambda + \int_0^{\infty} L_{Gas}(\lambda, T_{Gas})\, f(\lambda) d\lambda$$

$$I_{Photo} = I_{Photo,Wand}(T_{Wand}(t)) + I_{Photo,Gas}(T_{Gas})$$

The hardware setup is given in figure 20. The PYREX system was fixed by a thread at a single CMC ring segment component inside a standard copper chamber setup at a downstream position of completely formed combustion.

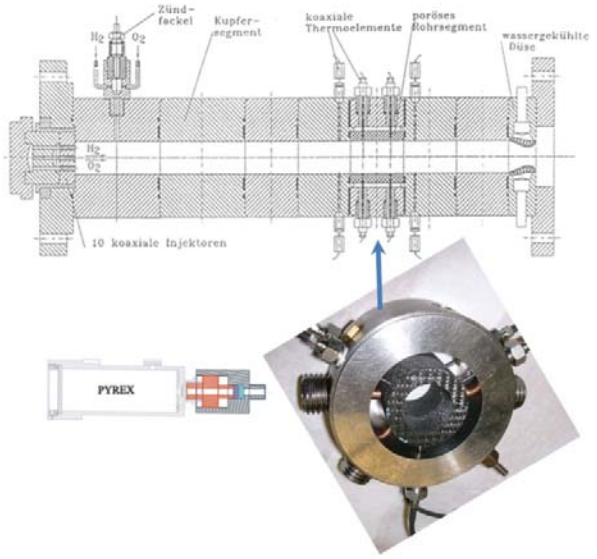

Fig. 20: Optical measurement setup for the CMC wall surface temperature in a standard DLR micro-combustor.

At the physical boundary conditions mentioned previously a relatively wide range of signal transparency (low absorption at 850 nm in H2-O2-combustion) allowed measurable signals for the detection of wall surface temperature (fig. 21).

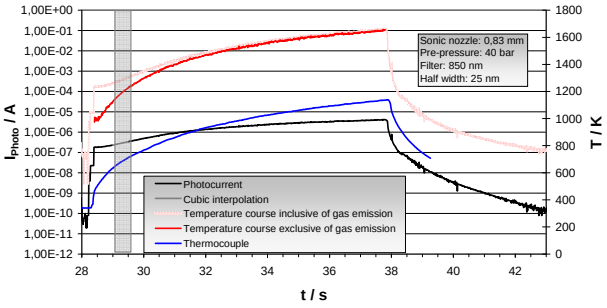

Fig. 21: Optical temperature measurement by 850 nm one-color pyrometer at 10 bar chamber pressure and a O2/H2 mixture ratio of 6.5.

The interpretation of the temperature curves immediately after extinction led to the assumption of effective wall surface temperatures around 1400 K. Unfortunately in following test campaigns these measurements could not be continued. The current goal now is to continue such measurements in future technology development for the installation of in-situ

health monitoring systems in conjunction with non-temperature-critical transpiration operated inner chamber walls.

IV Summary

The new dual-shell hyperboloid rocket combustion chamber design found its initiation in the long lasting cone injector development corresponding to DLRs transpiration cooled ceramic rocket thrust chamber development, a new arrangement of injector elements, or components respectively. The derived combustion chamber design shows of course higher weight and heat transfer surface compared to the classical rocket combustion chamber design. But using light-weight composite materials this disadvantage can be largely compensated. Apart from that it shows several advantages from the operational side.

A film cooled orbital propulsion system can be operated with slightly higher I_{sp}, but particularly at significant lower maximum surface temperatures ($\Delta T >$ 100 K) in the critical nozzle throat zone.

An expander cycle operated engine would profit from the use of the dual-shell hyperboloid chamber in two ways. On the one hand, caused by the increased inner wall surface, significantly more enthalpy can be transferred from the hot gas to the coolant, which results in more turbo pump power. The latter would increase the overall engine efficiency. On the other hand the entire stage can be built shorter, which reduces stage weight.

A gas generator design in a dual-shell hyperboloid shape could bring a more homogeneous temperature field in the exit plane, or in the turbine inlet respectively, without the need of additional distributor grids.

Finally the new design approach promises an increase in overall engine efficiency, applying the so-called injection-cooling-method in an I_{sp} optimal operation. Here the performance loss caused by substantial pressure losses in the pure chamber cooling system could be excluded to a large extent, because the chamber wall takes at once the function of the injector.

V Outlook

The next highly interesting investigation focus lies on the demonstration of the so-called injection-cooling-method. More detailed numerical simulations of mixing and combustion will be performed. Considering non-critical surface temperatures at the inner hot gas wall the application of optical sensors for reliable in-situ health monitoring systems seems to be easily feasible.

Apart from that, subscale demonstration tests shall be conducted to validate the theoretical predictions in all application scenarios mentioned before.

VI Acknowlegements

Our particular thanks apply for the DEPARTMENT of COMBUSTION SIMULATION at the INSTITUTE of COMBUSTION TECHNOLOGY (DLR Stuttgart), in persons Dr. Peter Ess and Dr. Peter Gerlinger for their scientific support concerning combustion processes.

VII References

[1] S. Michaelides, 2016. Ansys-CFX-Simulation einer keramischen Gasgenerator-Brennkammer fuer einen LOX/LCH4 Raketenantrieb der 35 kN Klasse. *Internal report ILR-RFS GB 16-07, Professur fuer Luft- und Raumfahrt at the Technical University of Dresden and Institute of Structures and design at DLR Stuttgart, Germany.*

[2] T. Schleutker, 2014. Analytischer und numerischer Vergleich des Wandwaermestroms bei konventionellen und hyperbolischen Brennkammern. *Diplomarbeit, Institute of Space Systems at the Technical University of Stuttgart and Institute of Structures and design at DLR Stuttgart, Germany.*

[3] H. Seiler, 2017. Structural design of the hyperboloid gas-generator combustion chamber for a 35 kN LOX/Methane rocket propulsion system. *Master work IRS-17-SO48, Institute of Space Systems at the University of Stuttgart and Institute of Structures and design at DLR Stuttgart, Germany.*

[4] M. Ortelt, A. Herbertz, H. Hald I. Müller. 2013. Advanced Design Concepts for Ceramic Thrust Chamber Components of Rocket Engines. *5th EUROPEAN CONFERENCE FOR AERONAUTICS AND SPACE SCIENCES, Munich, Germany.*

[5] A. Herbertz, M. Ortelt, I. Müller, H. Hald. 2012. Transpiration-Cooled Ceramic Thrust Chamber Applicability for High-Thrust Rocket Engines – Scaling of KSK Test Results. *48th AIAA/ASME/SAE/ASEE Joint propulsion Conference & Exhibit, Atlanta, Georgia.*

[6] M. Ortelt, A. Herbertz, H. Elsässer, H. Hald I. Müller. 2012. Structural Investigations on Cryogenically Operated and Transpiration Cooled Fiber Reinforced Rocket Thrust Chambers. *48th AIAA/ASME/SAE/ASEE Joint Propulsion Conference & Exhibit, Atlanta, Georgia.*

[7] M. Ortelt, F. Breede, A. Herbertz, D. Koch, H. Hald. 2013. Current activities in the field of ceramic based rocket engines. *ODAS 2013- 13th*

ONERA-DLR Aerospace Symposium, Palaiseau, France.

[8] A. Herbertz, M. Selzer. 2013. Analysis of Coolant Mass Flow Requirements for Transpiration Cooled Ceramic Thrust Chambers. 29*th International Symposium on Space Technology and Science, Nagoya, Japan.*

[9] M. Selzer, S. Schweikert. 2013. Transfer of an analytical transpiration cooling model to the cooling analysis of rocket combustion chambers made of ceramic matrix composites. *5th European Conference for Aeronautics and Space Scoences (EUCASS), Munich, Germany.*

[10] S. Gordon, B.J. McBride. 1994. Computer Program for Calculation of Complex Chemical Equilibrium Compositions and Applications. *Techn. Rep., NASA, USA.*

[11] A. Ponomarenko. 2017-03-30. RPA – Tool For Rocket Propulsion Analysis. *URL: www.propulsion-analysis.com.*

[12] T. Linder. 2014. Numerische Untersuchung von Transpirationsgekuehlvorgaengen mit Augenmerk auf die Kopplung zwischen Heiss- und Kuehlgasstroemung. *Bachelorthesis Institut fuer Thermodynamik der Luft- und Raumfahrt,. University of Stuttgart, Germany.*

[13] H.W. Coleman, B.K. Hodge, R.P.Taylor. 1984. A Re-Evaluation of Schlichting's Surface Roughness Experiment. *Journal of Fluids Engineering, Vol. 106.*

[14] M.M. Pimenta, R.J. Moffat, W-M. Kays. 1975. The Turbulent Boundary Layer: An Experimental Study of the Transport of Momentum and Heat with the Effect of Roughness. *Interim Report, Stanford University, CA.*

[15] Ansys, Inc. ANSYS CFX-Solver Modelling Guide 17.1. April 2016.

[16] M. Ortelt, H. Hald, I. Mueller; 2014. Status and future perspectives of the CMC rocket thrust chamber development at DLR. *65th International Astronautical Congress, Toronto, Canada.*

[17] S. Soller, B. Kniesner, C. Maeding, R. Kaess, R. Behr, A. Dahlaus, R. Blasi. 2013. Astrium's LOX/LCH4 Gas Generator Development Programme. *5th EUROPEAN CONFERENCE FOR AEROSPACE SCIENCES (EUCASS 2013)*. München, Germany.

[18] Educational Manuscript. Fluidreibungswiderstand an Oberflaechen. *URL: http://hydro.ifh.uni-karlsruhe.de/download/Kap07ps.pdf. University of Karlsruhe, Germany.*